

DYNAMIC MODELLING AND CONTROL OF AN AERODYNAMICALLY CONTROLLED CAPTURING DEVICE FOR ‘IN-AIR-CAPTURING’ OF A REUSABLE LAUNCH VEHICLE

Sunayna Singh⁽¹⁾, Sven Stappert⁽¹⁾, Sophia Buckingham⁽²⁾, Sylvania Lopes⁽²⁾, Yakut Cansev Kucukosman⁽²⁾, Madalin Simioana⁽³⁾, Mihai Pripasu⁽³⁾, Andreas Wiegand⁽³⁾, Martin Sippel⁽¹⁾, Philippe Planquart⁽²⁾

⁽¹⁾ *DLR Institut für Raumfahrtssysteme, Linzer Strasse 1, 28359, Bremen, Germany, Sunayna.Singh@dlr.de, Sven.Stappert@dlr.de, Martin.Sippel@dlr.de*

⁽²⁾ *von Karman Institute for Fluid Dynamics, 72 Chaussée de Waterloo, Rhode-St-Genèse B-1640, Belgium, sophia.buckingham@vki.ac.be, sylvania.lopes@vki.ac.be, yakut.cansev.kucukosman@vki.ac.be, philippe.planquart@vki.ac.be*

⁽³⁾ *Astos Solutions, Blvd. Alexandru Ioan Cuza 32a, 011055, Bucharest, Romania, madalin.simioana@astos.ro, mihai.pripasu@astos.ro, andreas.wiegand@astos.de*

ABSTRACT

The renewed interest in reusable launch vehicles has fueled the development of many advanced space transportation concepts. An interesting method for recovering rocket stages called ‘In-Air-Capturing’, has been patented by DLR. The winged stages are captured mid-flight and towed back to the landing site by an aircraft, eliminating the need for an additional propulsion system. A critical procedure in the capturing process involves an aerodynamically controlled capturing device attached by a rope to the towing aircraft, performing an autonomous rendezvous maneuver with the launch vehicle. In this paper, the complex dynamics associated with this phase are modelled and examined. This includes the aerodynamics of the capturing device, external disturbances like the turbulent wake of the aircraft and the flexible dynamics associated with the rope. These effects are combined into a multidisciplinary framework and a preliminary control system is proposed. The final open-loop simulation results provide valuable information about the stability and controllability of the system, which will be used for advanced control design in future work.

1 INTRODUCTION

The idea of Reusable Launch Vehicles (RLVs) has been a matter of interest ever since 1970s. The peak of this research gave rise to the first operational RLV - Space Shuttle. The shuttle, although a successful RLV, could not provide the cost benefit of re-usability. Today, in the very competitive environment, the reduction of launch cost has become a driving factor for the development of reusable launch technology. The currently operational and successful launch vehicles from SpaceX and Blue Origin are designed to land vertically. Return To Launch Site (RTL) and Down-Range Landing (DRL) require a significant quantity of fuel to perform a successful landing. Further, winged fly-back stages require an additional propulsion system to perform horizontal landing, which also adds to the stage mass. An innovative approach patented as “In-air-capturing (IAC)” [1], provides the possibility of returning a winged stage back to the launch site without the need for a propulsion system, thereby cutting down on the associated costs.

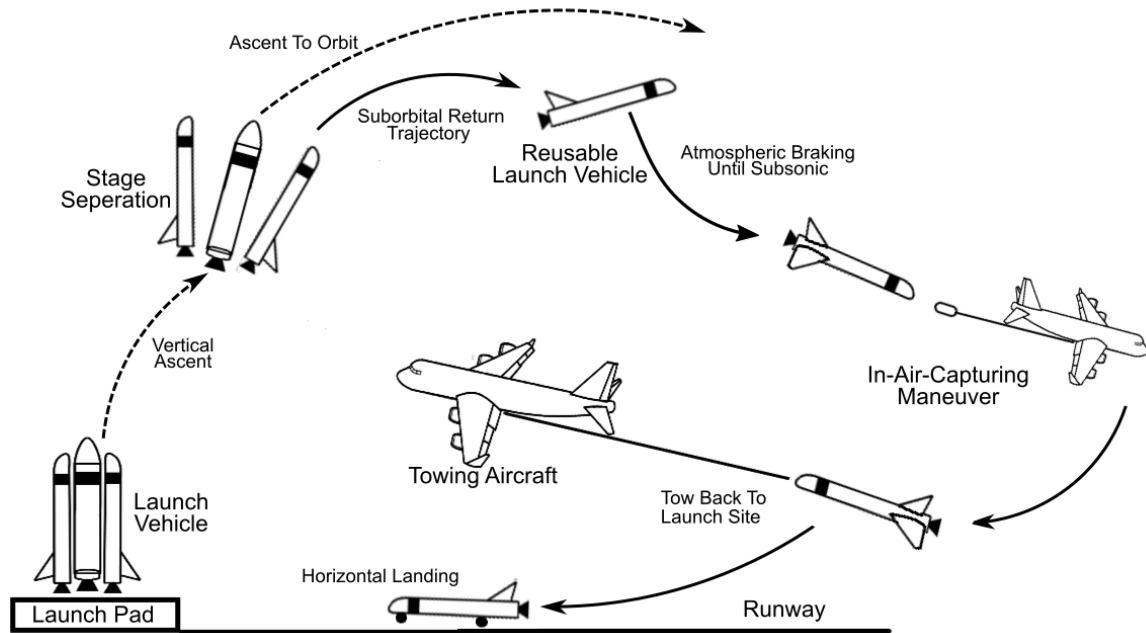


Figure 1: Complete IAC Cycle

Figure 1 shows a basic schematic of the complete operational cycle of IAC. After a vertical lift-off, the winged booster stage separates at Main Engine Cut-Off (MECO) and re-enters the atmosphere following a ballistic trajectory. At about 20 km altitude, it begins deceleration from supersonic velocity to a subsonic glide. Meanwhile, a Towing Aircraft (TA) loiters at 10 km altitude until the RLV reaches its vicinity. Between 8 km to 2 km, the IAC maneuver is performed [2]. The aircraft glides into a parallel formation with the RLV, such that the two vehicles have similar velocities and flight-path angles. During this formation flight, an Aerodynamically Controlled Capturing Device (ACCD) attached by rope to the aircraft, autonomously captures the RLV. Then, the TA tows it back to the landing site [3]. In the vicinity of the runway, the stage is released to perform a horizontal landing.

The IAC method can be used for retrieval of not only returning launcher stages, but also smaller parts like fairings. The launcher stages themselves can vary in size, which would in turn influence the size of the commercial aircraft selected for towing. However, for the current study a full-scale or large scale scenario for IAC is considered. For this the selected vehicles are as follows:

- **Reusable Launch Vehicle (RLV):** Since typical commercial aircraft have a high Lift-To-Drag (L/D) ratio, the same should be maximised in RLV to allow successful formation. But a high L/D is usually achieved by increasing the wing span and size, which in turn decreases the payload capability. Therefore, a swept wing configuration was proposed to achieve a viable compromise between both requirements. The winged RLV configuration shown in Fig. 2a is the first stage for a 3 Stage-To-Orbit (3STO) launch vehicle (more details can be found in [4]). The stage mass during the descent is approximated to be about 80 tons.
- **Towing Aircraft (TA):** Based on the thrust requirements for towing a large RLV stage, a four engine, long range jetliner like the A340-600 was deemed fit [3]. The retired aircraft comes with powerful Rolls Royce Trent 556 engines and large loading capacity to support the towing loads. It also has a relatively advanced flight control system that makes it suitable for IAC.

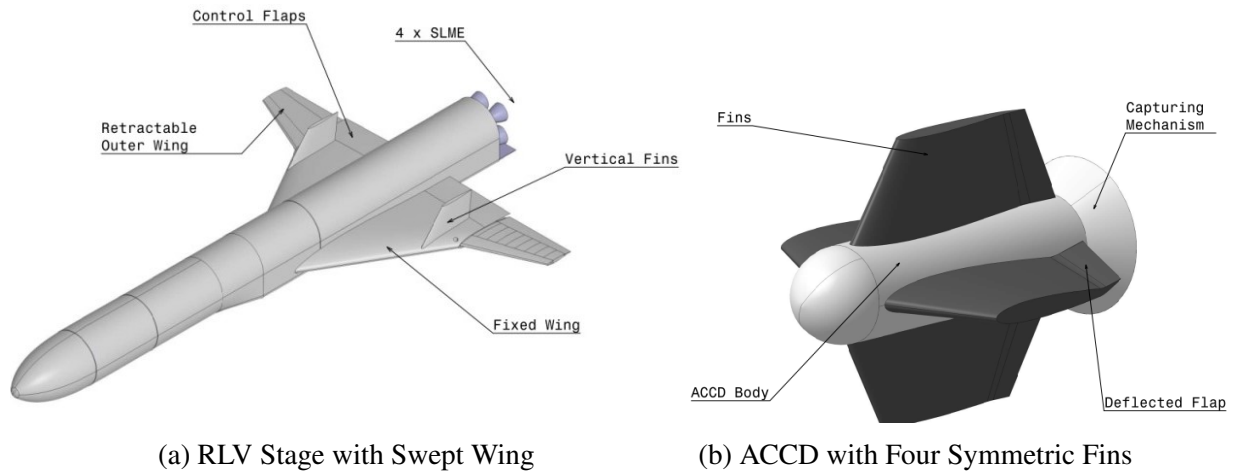


Figure 2: Selected Test Configuration for Full-Scale Simulation

- **Aerodynamically Controlled Capturing Device (ACCD):** This device is critical for the successful capture of RLV. For the current study, the ACCD is 2 m long with a cross-sectional diameter of 1.5 m, including the fins as shown in Fig. 2b. The four large fins, which can deflect up to a maximum of $\pm 15^\circ$ provide 6DOF agility and control. The nose of the ACCD is attached to the TA via rope and the back cone of the ACCD secures the connection with the RLV.

The current paper will present the modelling and analysis of the capture phase, wherein the ACCD navigates its way to the RLV to establish a secure connection, while the TA and RLV remain in formation flight. To achieve this, the ACCD must overcome significant disturbing forces like wake from the towing aircraft and flexible perturbations from the rope. Since the ACCD is only controlled aerodynamically using its fins, understanding the effect of these dynamic interactions becomes essential for control design. Therefore, the coming sections will provide an overview of these critical aspects of dynamics and the overall modelling approach. Further, the open-loop response of the system will be analyzed and a control architecture will be proposed.

2 SIMULATION MODEL

Figure 3 shows the closed-loop framework for simulation of capture phase. The TA trajectory acts as a constraining state for one end of the rope, while the RLV trajectory acts as the commanded state to the system. The plant model includes the environment model, aerodynamic forces, disturbing forces as well as equations of motion to the system. The ACCD state, which is highly coupled with the rope dynamics is compared against the state of the RLV. The controller then generates an output to correct for this difference, which is translated to ACCD flap deflections and fed back to the plant.

In this section, some critical aspects of the model are discussed in further detail. Since the ACCD is aerodynamically controlled, the model demands extensive high fidelity data to be able to adequately represent the dynamics. Additionally, the wake generated from the aircraft can cause considerable disturbances to the rope and consequently, also the ACCD. Hence, the aerodynamic modelling and characteristics of the system are discussed in Sec. 2.1. Simulation of a closed-loop system with flexible dynamics requires careful selection of modelling approach. This is to ensure that the dynamics of the system are represented adeptly without a large penalty on computation time. Thus, Sec. 2.2 explains the multibody rope methodology used to represent the flexible dynamics of the system. Lastly, a control architecture for 6DOF control using only the four fins of ACCD is proposed in Sec. 2.3.

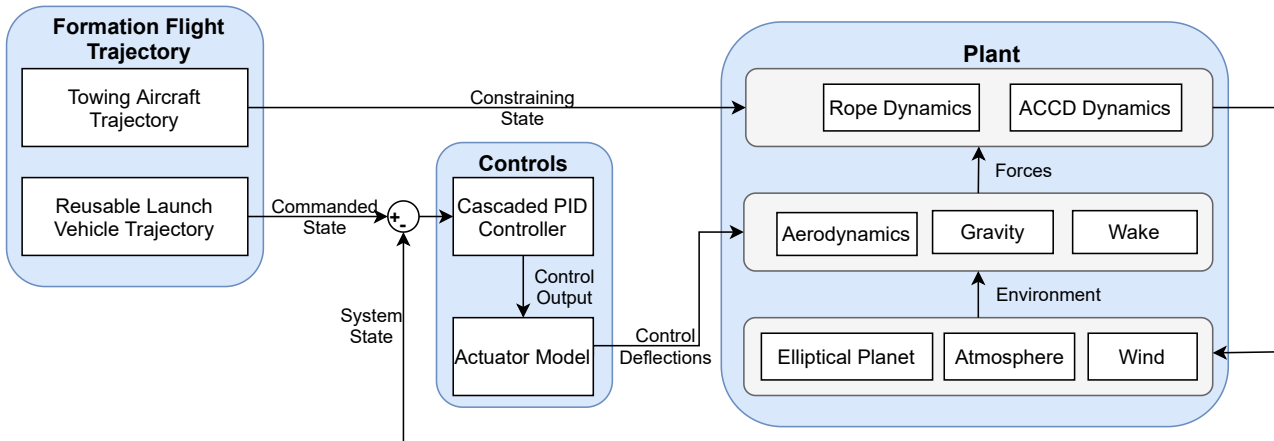


Figure 3: Simulation Framework

2.1 Aerodynamic Characterisation of the System

Computational Fluid Dynamics (CFD) is used to provide an in-depth characterization of the steady 3D flow field around the ACCD. Firstly, the numerical specifications for the simulation are defined. This is followed by a critical review of the preliminary ACCD design, placing particular emphasis on examining its stability and controllability. Finally, a full-scale 3D simulation of the wake originating from the TA is analyzed and presented. The resulting disturbance field will be integrated into the multi-body simulation framework.

2.1.1 Numerical methodology

The methodology followed to reach a high confidence level in the numerical CFD results is summarized hereafter. The open source code OpenFOAM v6.0 [5] is used to perform Reynolds-Averaged Navier Stokes (RANS) simulations of the ACCD and the TA. The *rhoSimpleFoam* solver was selected to describe the compressible/subsonic flow regime of interest. Several turbulence models were tested on a simplified model (NACA 0012 airfoil) in a similar regime (Mach no. 0.6, Reynolds no. 9×10^6), to determine the most appropriate model for these flow types. As a result of this sensitivity analysis, $k-\omega$ SST turbulence model was chosen for its ability to accurately predict separated flow areas.

Since the ACCD will be exposed to the wake of the TA during capture, an investigation of the turbulence intensity effects on the aerodynamic coefficients was also performed. The CFD simulation of the TA indicates that the ACCD is likely to be exposed to a turbulence intensity in the order of 5% or less during the capture manoeuvre. Therefore, three different inflow turbulence intensities (0.5%, 1% and 5%) were tested and the results showed no influence of the turbulence intensity, in this range, on

Table 1: Simulation Flight Point

Velocity [m/s]	142.39
Mach	0.45
Altitude [m]	6000
Pressure [Pa]	47248.92
Density [kg/m ³]	0.66065

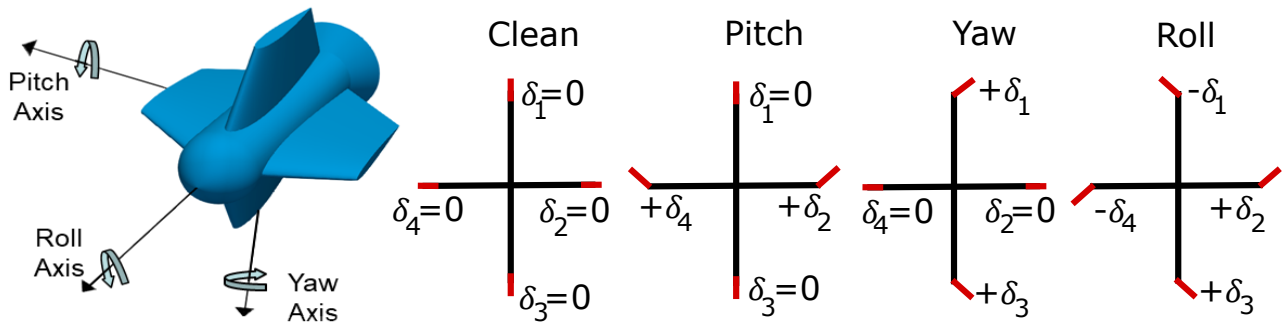


Figure 4: Sign Conventions for ACCD Flap Deflection and Resulting Moments

the aerodynamic coefficient values. The size of the numerical domain was adjusted in order to reduce the influence of the boundary conditions and set at conservative distances of $5 \times L_{ref}$ and $10 \times L_{ref}$ in the upstream and downstream directions respectively, where $L_{ref}(=2 \text{ m})$ corresponds to the body's reference length. An independent mesh sensitivity study was performed in either case to ensure that an accurate yet computationally effective grid resolution is chosen.

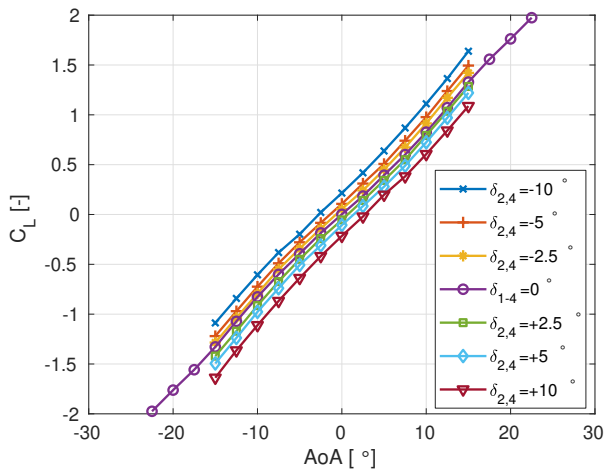
All the numerical simulations of the ACCD are performed for its main flight operational point, for which characteristics are listed in Table 1. Figure 4 shows how roll, pitch and yaw deflections are realized using the four flaps. For pitch, both horizontal flaps deflect in the same direction. For yaw, both the vertical flaps are deflected in the same direction. And for roll, all flaps are deflected as shown in Fig. 4. These symmetric configurations of flap deflections up to 10° for pitch, yaw and roll motion were simulated for the range of $\pm 15^\circ$ Angles of Attack (AoA).

2.1.2 ACCD aerodynamic performance and stability

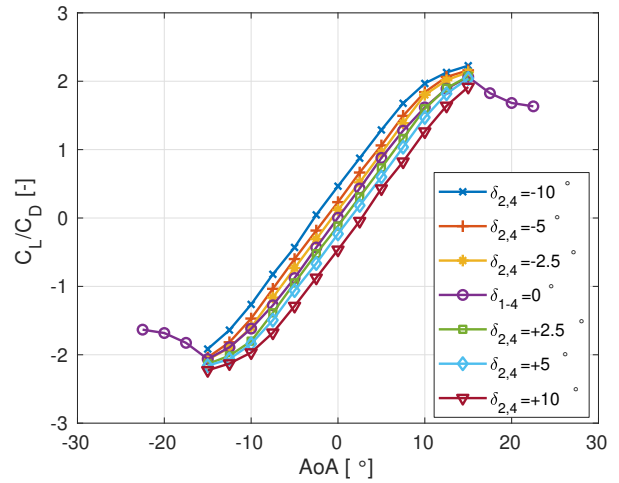
A critical review of the preliminary ACCD design has been performed to identify potential design improvement, and satisfy the requirements for aerodynamic performance and stability. The ACCD aerodynamic performance during pitch maneuvers is presented in Fig. 5. The lift coefficient curves show linear growth with AoA over the whole range. In Fig. 5b, the efficiency curves, defined by the ratio of lift and drag coefficients, reach an absolute maximum of approximately 2 at 15° AoA, independent of the flap deflection. Above this AoA, a drop in the efficiency, due to the big increase in the C_D (while the C_L grows linearly), is observed for the base condition (no flap deflection).

As it can be seen in Fig. 5c and Fig. 5d, the slopes of the pitch moment coefficients are negative and the positions of the Aerodynamic Center (AC) are located behind the center of gravity (for positive angles of attack and negative fin deflection; and negative angles of attack and positive fin deflection). This indicates that the selected Center of Gravity (CoG) located 0.6 m from the nose gives a stable ACCD configuration. The negative slope of the pitch moment coefficient indicates static stability such that, if AoA increases, the pitch moment brings back the device to equilibrium.

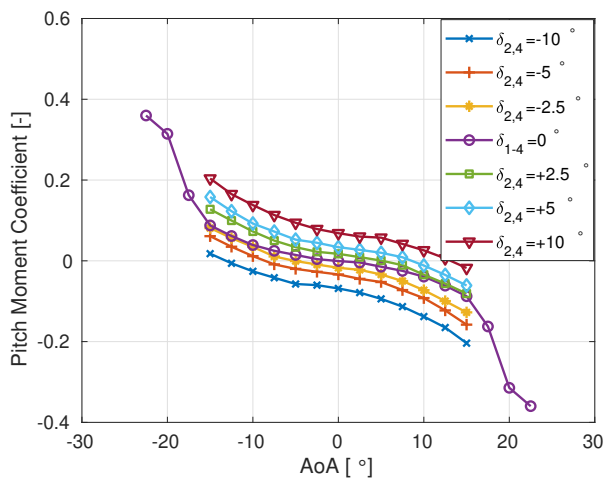
The yaw and roll flap deflection cases have little to no effect in the aerodynamic performance of the ACCD, as seen in Fig. 6a. This is due to the fact that the vertical flap deflection has no influence on the lift and only a small contribution to the drag force. Also, the roll cases equalize the pressure distribution inducing no extra lift. The roll flap deflection cases also have a very small effect on



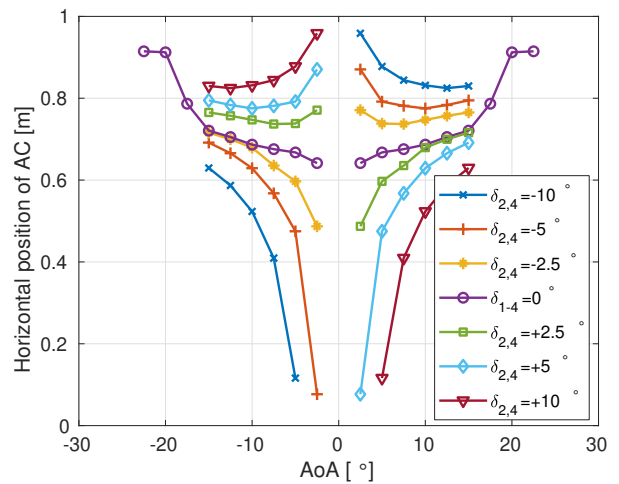
(a) Lift Coefficient



(b) Aerodynamic Efficiency

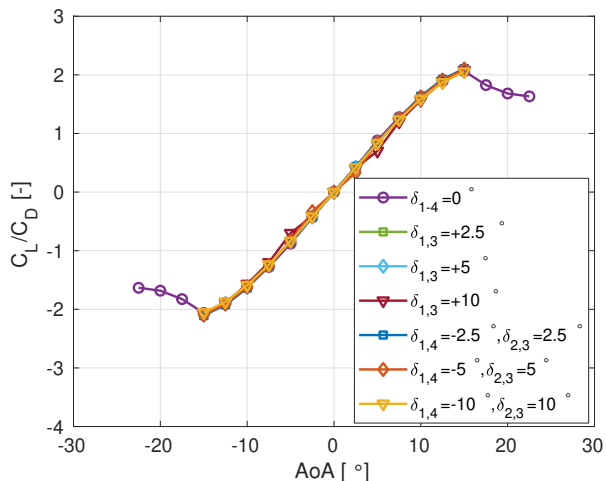


(c) Pitch Moment Coefficient for CoG=0.6m

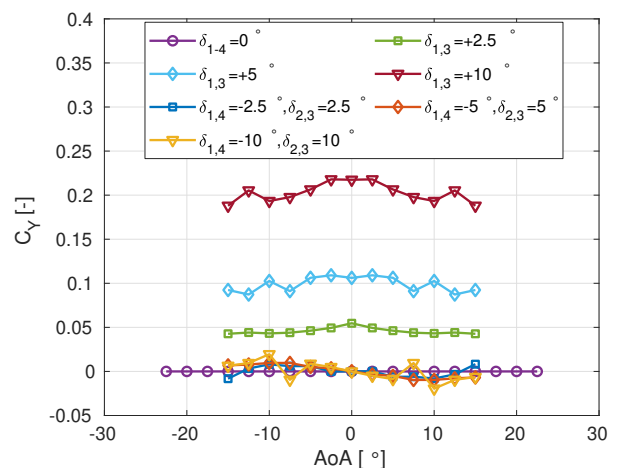


(d) Horizontal Position of the AC for CoG=0.6m

Figure 5: ACCD Aerodynamic Coefficients for Pitch Maneuver



(a) Aerodynamic Efficiency



(b) Side Force Coefficient

Figure 6: ACCD Aerodynamic Coefficient for Yaw and Roll Maneuver

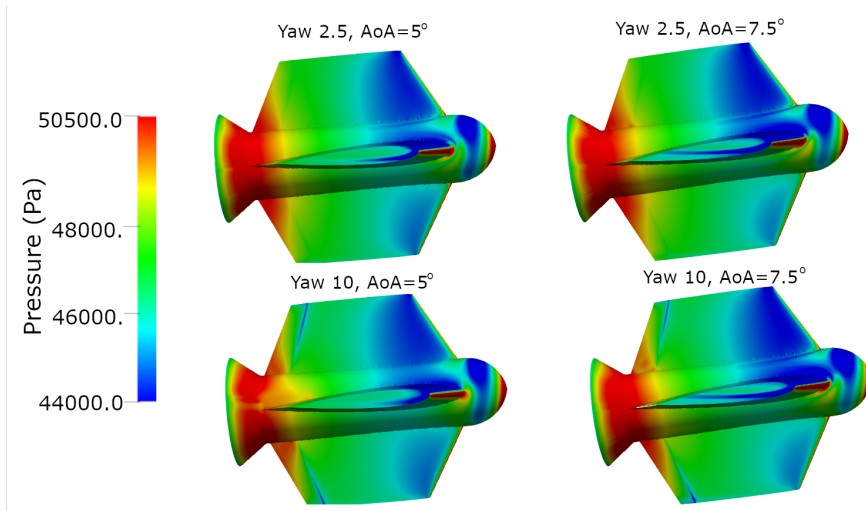


Figure 7: Pressure Contours on the ACCD Leeward Side for Yaw Maneuver

the side force coefficient, as shown in Fig. 6b. The vertical flap deflection increases the side force coefficient as expected. The small jump of the side force coefficient for AoA above 7° for higher fin deflection are possibly due to the increase of shadowing effects resulting in asymmetric pressure distribution. The upper vertical fin becomes more shadowed and the force component in the side direction, induced by suction pressure at the leeward side becomes weaker at the opposite lower fin. This behavior can be observed in Fig. 7, where the contours of the surface pressure are shown. As it can be seen, the pressure distribution on the fin surfaces on the leeward side is symmetric between the upper and the lower vertical fin at 5° and 7.5° AoA for a flap deflection of 2.5° . However, it becomes asymmetric already at 7.5° AoA (and for the subsequent higher AoAs) for flap deflection of 10° .

2.1.3 Wake analysis downstream of the towing aircraft

The numerical approach described in Section 2.1 is applied to simulate the 3D flow-field around the A340 towing aircraft in order to extract the wake field of interest for the IAC approach. A symmetric boundary condition is applied to the central vertical plane to reduce computational efforts. In addition, the engines are modeled in a simplified way, whereby the rotating parts are replaced by a momentum source to replicate thrust and the velocity is increased by 10% at the engine outlet. In this configuration, the landing gear is deployed together with the spoilers at 20° so as to decrease the L/D ratio and enable formation between the TA and the RLV.

The wake results are presented in the fuselage plane where the ACCD will likely remain during the capture maneuver. Contour plots of velocity magnitude at AoA = 0° & 6° can be found in Fig 8, where profiles are extracted at the indicated streamwise positions and plotted in Fig. 9. Profiles of streamwise and downwash components of velocity normalized by the free-stream value, are included. The turbulent kinetic energy k , which corresponds to the root mean square of the turbulent fluctuations in velocity, is representative of the turbulence level in the wake [6]. While the streamwise velocity and kinetic energy is of very similar amplitude between the AoA cases, it shifts downwards at AoA = 6° due to incidence. A negative downwash velocity component is observed for the fuselage region in case of 0° AoA. However, the downwash velocity component is more pronounced at higher AoA, which is around 8% of the freestream and up to 1.5 fuselage length ($L_{ref} \approx 76$ m) downstream from the aircraft. This part of the wake could be potentially problematic for the stability of the ACCD and

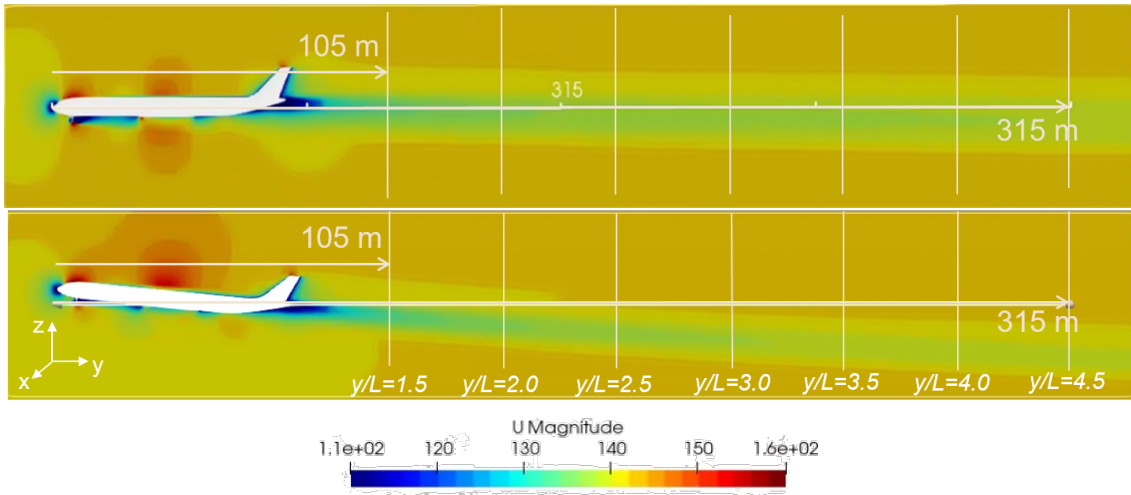


Figure 8: Wake Velocity Magnitude Contours for AoA of 0° (top) and 6° (bottom).

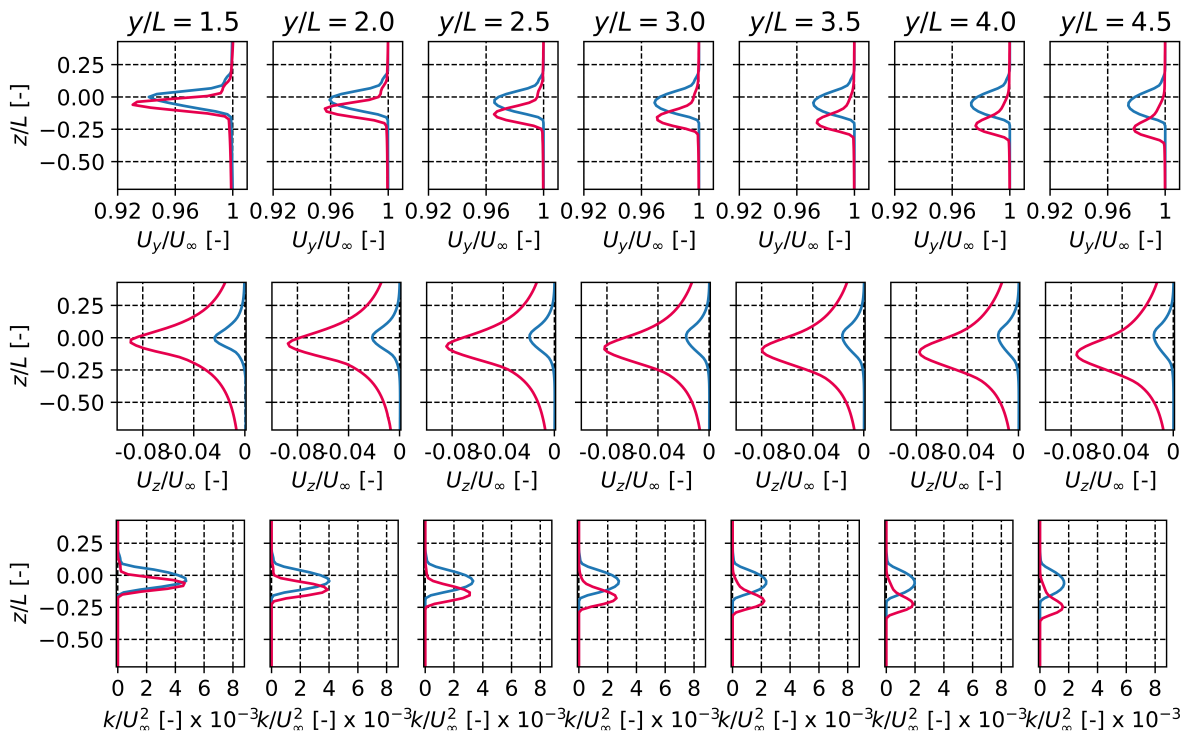


Figure 9: Wake Profiles in the Fuselage Plane; Streamwise Velocity Component (top), Downwash Velocity Component (middle) and Turbulent Kinetic Energy (bottom) for 0° (blue) and 6° (red) AoA.

could be avoided by placing the ACCD further below the A340. In conclusion, the optimal placement of the coupling device is highly dependent on the AoA of the aircraft since it influences the velocity profiles in the vertical direction.

2.2 Multibody Rope Dynamics

Many factors come into picture while modelling the rope dynamics. Firstly, the rope must be able to withstand the loads from towing the RLV with minimal elongation. Secondly, the model should allow representation of rigid elements, like the TA and the ACCD attached at the end nodes of the rope. It should also account for external forces like the aerodynamics and wake perturbations acting on the rope. Lastly, the model should provide a good balance between accuracy and computation time for closed-loop control simulations. Owing to all these factors, a multibody modelling approach is selected for the dynamics. In this section, some important aspects of the rope model are presented.

2.2.1 Rope Material

The IAC application requires a durable and lightweight rope to endure towing forces. Therefore, a stable high strength fiber rope featuring extremely low stretch made with Ultra-high-molecular-weight polyethylene (UHMWPE) fibers is selected. The material is widely used for marine, sports, medical as well as space applications [7]. The ropes are known to be lightweight and possess good vibration damping properties. The rope can withstand massive forces, exceeding the strength of a steel wire rope with corresponding abrasion resistance. This permits a one-to-one substitution at the same diameter without the need for converting or adapting the periphery - at only 1/7 of the weight. The overall rope characteristics used in the multibody flexible model are presented in the Table 2.

Table 2: Rope Characteristics

Length [m]	225
Mass [kg]	28.125
Diameter [m]	0.014
Poisson's Ratio	0.46
Young's Modulus [GPa]	87
Damping Coefficient	0.02

2.2.2 Towing rope model

For the simulation of IAC, a discretized approach provides a good trade-off between accuracy and computation time. Thus, the rope can be modelled with n constrained equal rigid bodies linked together [8] as shown in Fig. 10a. Each body (rope segment) has a length l and mass m , such that the total rope mass is the sum of the mass of every segment. Identical springs with stiffness k_T are placed at each joint. Here, the constrained end of the rope is attached to the TA and the free end is attached to the ACCD. For a detailed modelling of the rope, four important properties are taken into account:

1. *Bending Stiffness*: The bending stiffness is the resistance of a material against bending deformation. The bending of a rope can be virtually represented using the radius of curvature (R), between two adjacent members as shown in Fig. 10b. Considering a basic formula of strength of materials, the relation between the radius of curvature R of a beam and the bending moment M is given by [8]:

$$\frac{1}{R} = \frac{M}{K} \quad (1)$$

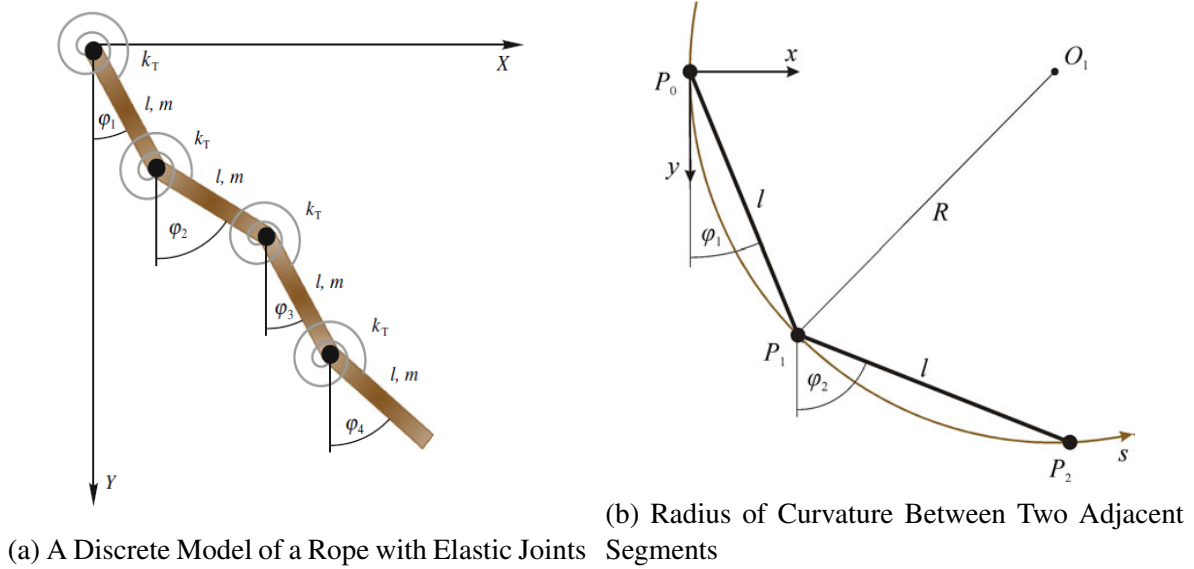


Figure 10: Modelling Approach for the Towing Rope [8]

where K is the flexural rigidity of the rope. Considering the geometrical relation in Fig. 10b, the curvature can be expressed as:

$$\frac{1}{R} = -\frac{2}{l} \frac{\tan \frac{\phi}{2}}{\cos \frac{\phi}{2}} \quad (2)$$

where ϕ is the relative angle between rope segments and l the length of a single segment. The elastic moment produced by the spring at the rope segments hinge is then defined as:

$$M = \frac{K}{R} = -K_b \cdot 2 \frac{\tan \phi/2}{\cos \phi/2} \quad (3)$$

where K_b is the bending stiffness value that can be computed as follows:

$$K_b = \frac{EJ}{l} \quad (4)$$

Here, E is the Young's modulus and J is the area moment of inertia of the cross-section.

2. *Torsional Stiffness*: The torsional stiffness is the resistance of a material to twisting. Assuming torsional deformation only occurs at the joints, the following equation is defined at each hinge:

$$T = K_t \varphi \quad (5)$$

where T is the torque, φ the twist angle and K_t the torsional stiffness given by:

$$K_t = \frac{E J_p}{2(1 + \sigma) l} \quad (6)$$

where J_p is the polar area moment of inertia and σ the Poisson's ratio.

3. *Axial Stiffness*: The axial stiffness is the resistance of a material against axial deformation. A single axial linear spring is added at one end of the rope to simulate the elastic elongation, while keeping the computation time reasonable. The axial stiffness coefficient for a rope with length l_{tot} and cross-section area A is given by:

$$K_a = \frac{EA}{l_{tot}} \quad (7)$$

4. *Damping*: Damping is the ability of a mechanical system to resist oscillatory behaviour. Damping is critical for smooth simulation and for accurate modelling of the rope dynamics. Therefore, a viscous damper at each rotational joint is defined with the Rayleigh's function:

$$M = -c\dot{\theta} \quad (8)$$

where c is the damping coefficient and $\dot{\theta}$ the relative velocity between the two nodes.

Taking these properties into consideration, the rope with a total length of 225 m is divided into 30 equal segments. The properties of each segment are summarized in Table 3.

Table 3: Properties of a Rope Segment

Length [m]	7.5
Area moment of inertia [m ⁴]	1.89×10^{-9}
Polar area moment of inertia [m ⁴]	3.77×10^{-9}
Bending stiffness [Nm/rad]	21.87
Bending damping [Nms/rad]	8.12×10^{-6}
Axial stiffness [N/m]	17.85×10^5
Axial damping [Ns/m]	51.8

2.3 Control Architecture

The capture window for the ACCD during which the RLV and the TA remain in formation, is estimated to be about 3 mins [3]. During this period, the ACCD should be able to perform multiple capture attempts if required. Thus, for effective control of ACCD, the controller should drive the device to the commanded state of RLV in the presence of external disturbances within a short time. This is to be achieved using the four aerodynamic surfaces, as previously shown in Fig. 4. Since the axial motion of ACCD is constrained by the rope, the main motion requirements lie in the YZ-plane. In this Section, a preliminary control architecture will be proposed based on these requirements.

Considering the axisymmetric geometry of ACCD and its actuators, the system can be considered very similar to a missile. This means only three moments, rolling (Δp), pitching (Δq) and yawing (Δr) can be used to control the body [9]. These control rates when translated to the body, produce the required forces and moments for movement in YZ-plane:

Roll Control Rate :	$+\Delta p \rightarrow +\Delta L$	Rolling Moment
Pitch Control Rate :	$+\Delta q \rightarrow +\Delta N$	Normal Force
Yaw Control Rate :	$+\Delta r \rightarrow +\Delta Y$	Side Force

Taking all these factors into consideration, a control architecture is proposed as shown in Fig. 11. It consists of a roll rate damper, to maintain a steady orientation. The pitch and yaw control is performed in two loops. The outer loop translates the commanded YZ position and orientation into a modified command based on the roll orientation of the system. The inner loop then uses these modified commands to generate the required control moment for the maneuver. Hence, the overall concept is based on Cascaded PID Control. Further, filters may be used based on the effect of rope perturbations and other disturbances of ACCD. For this, the dynamics of the system must be accurately modelled and studied. Therefore, the results will provide further outlook on what may be required for such a system.

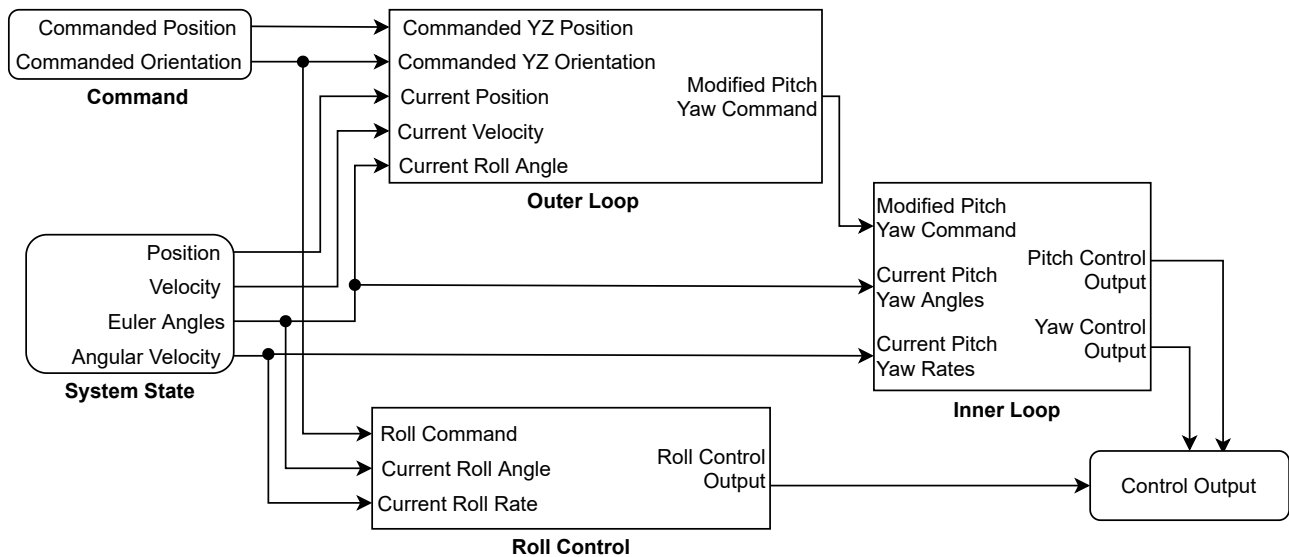


Figure 11: Proposed Control Architecture

3 RESULTS

Using the detailed aerodynamics and multibody rope models presented in Section 2 in the simulation environment shown in Fig. 3, a complete dynamic model is created. To examine the dynamics in detail some open-loop simulation results are presented in this section. The system in the uncontrolled condition provides a check for the stability of the rope dynamics, the definition of the simulation environment as well as the controllability of the ACCD. The preliminary simulations are performed in cruise conditions (levelled flight), keeping constant altitude and velocity of the TA, at the flight point shown in Table 1. Some critical aspects like effect of wake, vibrations due to the rope, contact forces and sensitivity to length of rope will be analyzed.

The A340-600 in the simulation is assumed to have a constant mass of 225 tons. The ACCD, which is connected to the aircraft with a 225 m long rope, weighs 164.5 kg. Given that the simulation starts at a levelled flight and is uncontrolled, the ACCD starts with an initial angle of attack of 10° in order to minimize the oscillatory behaviour. This behaviour would be introduced by initial loss in the altitude of the ACCD due to lack of normal force at 0° AoA. To check the disturbing effect of aircraft wake

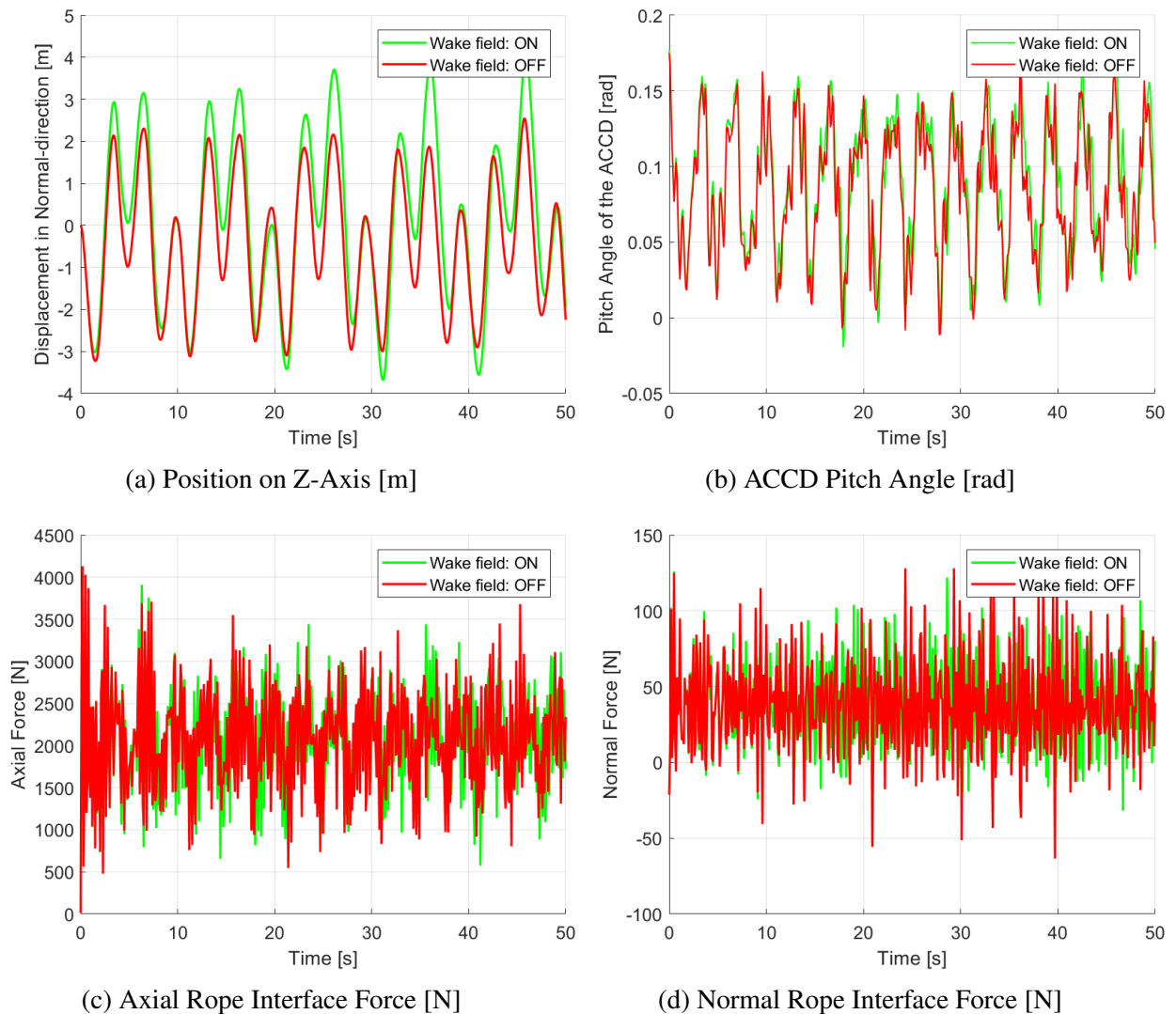


Figure 12: Sensitivity of ACCD to Wake Perturbations (Rope Length = 225 m)

on the rope and the ACCD, simulations were performed with and without the perturbing force.

Looking into the position of the ACCD in normal (Z) direction, shown in Fig. 12a, it appears to be on a stable profile with some oscillations. The oscillating frequency appears to be similar for both with and without wake. However, it appears that with wake, the amplitude of vibrations slightly increases (up to 3.8 m) as compared to the simulation without wake (up to 3 m). Similar observations can be made also in the pitch attitude of the ACCD shown in Fig. 12b. The effect of wake can be further understood by analyzing the rope interface forces, as shown in Fig. 12c and Fig. 12d. These forces do not seem to be significantly amplified by the presence of the wake field in both axial and normal direction. Based on these observations, the first conclusion will be that the effect of the wake field has a very limited impact when the rope is fully deployed to 225 m. From the frequency and amplitude of vibrations in the position and attitude, it can also be noticed that the vibrations do not appear to damp out over time. The low frequency vibrations can cause problems since they cannot be filtered out by standard filters in the control system. Dealing with these vibrations would require either a larger structural damping in the rope model, or active damping in the control system.

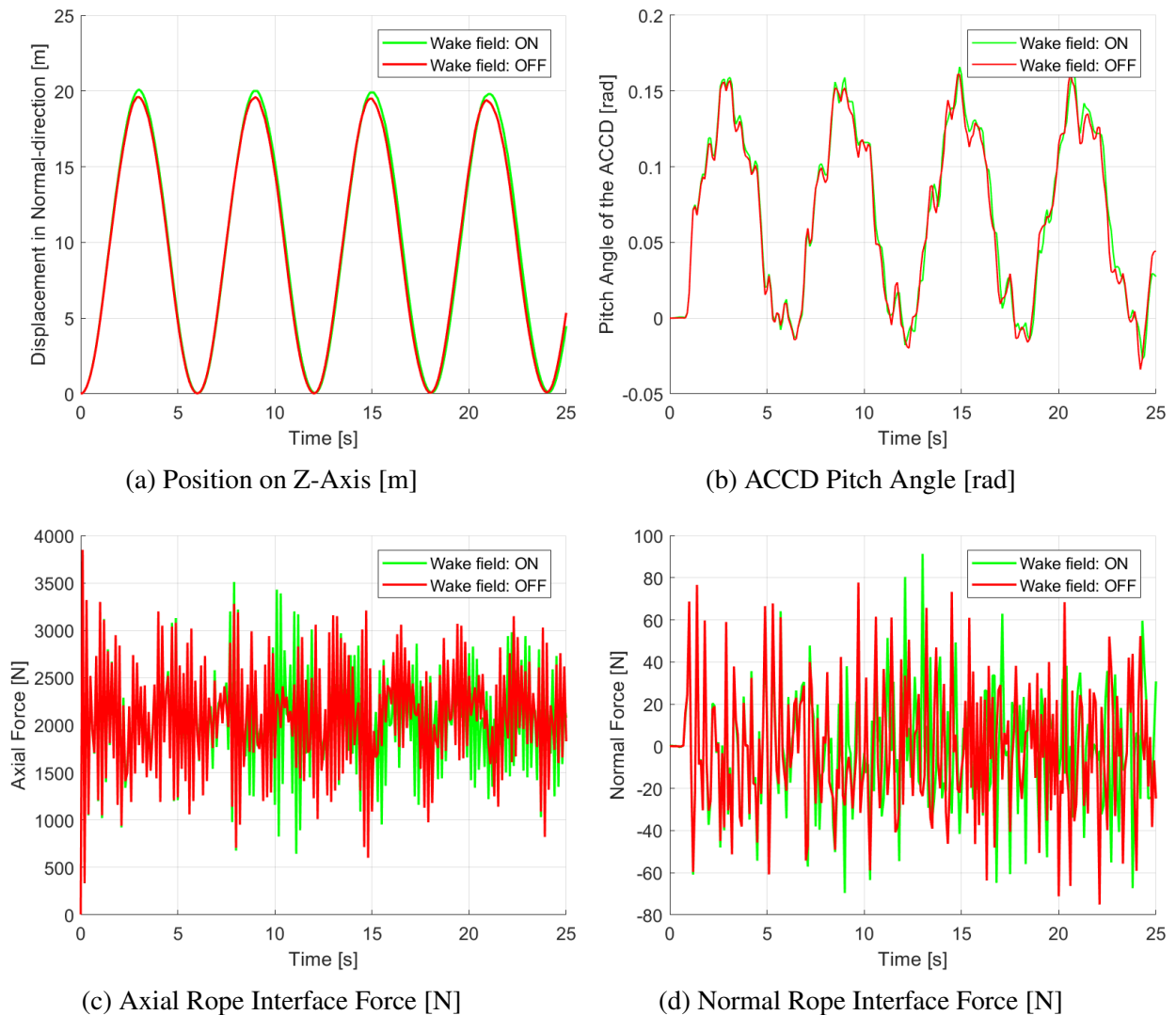


Figure 13: Sensitivity of ACCD to Wake Perturbations (Rope Length = 100 m)

To further verify the effect of wake, the rope is shortened to 100 m. Closer to the TA, the effect of wake is expected to be larger. Another factor that can be analyzed is the extent of vibrations when an initial oscillation is introduced. For this, the initial AoA for the ACCD is set to 0° . The increased initial oscillation will be a result of the loss in altitude due to lack of lift. From Fig. 13a and Fig. 13b, the ACCD displacement in Z-direction and the pitch attitude do not seem to show significant differences, with and without wake. However, the amplitude of vibrations are now much higher (up to 20 m displacement and 8.5° pitch angle) compared to the case when the rope is fully deployed. The large amplitude, low frequency vibrations are most likely caused by the initial disturbance due to 0° AoA. However, the high frequency vibrations in pitch angle may be originating from the natural frequency of rope. From Fig. 12c and Fig. 12d, the rope interface forces show that the amplitude of forces increase in some regions of the flight. But the increase is not significantly larger than the flight without wake. Therefore, it can be concluded again that the wake field does not impact the stability and controllability of the ACCD at the selected rope length and flight regime.

Conclusion

This paper demonstrates the detailed dynamic modelling for the application of IAC. Using high fidelity aerodynamics, it was confirmed that the ACCD design remains statically stable within the flight regime and produces the required aerodynamic forces for control using its flaps. Additionally, a multibody rope model suitable for closed-loop simulations was proposed and tested in the presence of turbulent wake from the aircraft. From the results, it was concluded that the wake does not have a significant disturbing effect on the dynamics of the system, when the rope is deployed at full length. A requirement for additional damping in the system was also identified.

The future research will include closed-loop simulations using the proposed control model. These simulations will involve ACCD performing a rendezvous maneuver with the RLV. Additional filters and active dampers may be included in the model based on the closed-loop dynamics. Multiple failure scenarios and sensitivity to factors like signal delay, noise and so on, will also be examined.

Acknowledgements

This work was performed under the Horizon 2020 project ‘Formation flight for in-Air Launcher 1st stage Capturing demonstration’ (FALCon) aimed at development and testing of the “In-Air-Capturing” technology. FALCon, coordinated by DLR-SART, is supported by the EU within the Programme 5.iii. Leadership in Enabling and Industrial Technologies – Space with EC grant 821953. Further information on FALCon can be found at <http://www.FALCon-iac.eu>

REFERENCES

- [1] DLR, “Verfahren zum bergen einer stufe eines mehrstufigen raumtransportsystems,” Patent DE 101 47 144 C1, released 2003.
- [2] M. Sippel and J. Klevanski, “Progresses in simulating the advanced in-air-capturing method,” in *5th International Conference on Launcher Technology, Missions, Control and Avionics S*, vol. 15, 2003.
- [3] M. Sippel, S. Stappert, L. Bussler, S. Krause, S. Cain, J. Espuch, S. Buckingham, and V. Penev, “Highly efficient rlv-return mode “in-air-capturing” progressing by preparation of subscale flight tests,” in *8th European Conference For Aeronautics And Space Sciences (EUCASS)*, Madrid 2019.

- [4] S. Stappert, J. Wilken, L. Bussler, and M. Sippel, “A systematic comparison of reusable first stage return options,” in *8th European Conference For Aeronautics And Space Sciences (EUCASS)*, Madrid 2019.
- [5] C. J. Greenshields, *OpenFOAM User Guide*. OpenFOAM Foundation Ltd., 2018, vol. 6.
- [6] L. Xiaofeng and T. O. Flint, “Measurement of the turbulent kinetic energy budget of a planar wake flow in pressure gradients,” *Experiments in Fluids*, vol. 37, no. 4, pp. 469–482, 2004.
- [7] H. L. Stein, “Ultra high molecular weight polyethylene (uhmwpe),” *Engineering Materials Handbook*, vol. 2, pp. 167–171, 1988.
- [8] P. Fritzkowski and H. Kaminski, “Dynamics of a rope modeled as a multi-body system with elastic joints,” *Computational Mechanics*, vol. 46, pp. 901—909, 2010.
- [9] P. H. Zipfel, *Modeling and Simulation of Aerospace Vehicle Dynamics*. American Institute of Aeronautics and Astronautics, 2007.